



# The Impact of Bogie Sections on the Wake Dynamics of a High-Speed Train

Zhiwei Zhou<sup>1,2</sup> · Chao Xia<sup>1,2</sup>  · Xizhuang Shan<sup>1,2</sup> · Zhigang Yang<sup>1,2,3</sup>

Received: 21 January 2019 / Accepted: 10 July 2019 / Published online: 27 July 2019  
© Springer Nature B.V. 2019

## Abstract

The impact of bogie sections on the wake dynamics of a high-speed train (HST) is numerically explored using the improved delayed detached eddy simulation (IDDES). Time-averaged and instantaneous wake flow topology are compared for two underbody configurations: the complex train model (CTM) with bogie sections and the simplified train (STM) with a flat underbody. For both underbody configurations, a pair of counter-rotating half-loop vortices dominates the unsteady wake. Each member of the vortex pair is shed alternately in the wake of the CTM, which is attributed to vortex shedding from the bogie sections. While for the STM, the members of this vortex pair couple and appear simultaneously. The dynamic characteristics of the wake are clarified by using proper orthogonal decomposition (POD) analysis for the IDDES results. The first four POD modes, corresponding to the dominant vortex structures, are analysed in detail, which confirms the significant impact of bogie sections on the wake dynamics of a HST.

**Keywords** Train aerodynamics · Wake dynamics · IDDES · POD

## 1 Introduction

The wake of a modern high-speed train (HST) is highly three-dimensional and unsteady [1, 2]. It is generally recognized that a pair of counter-rotating symmetric streamwise vortices dominates the wake of a HST from the time-averaged point of view. This streamwise vortex pair moves downwards and outwards as it progresses away from the tail train due to mutual induction and interaction with the image pair [2]. The slipstream velocity peak in the near

---

✉ Chao Xia  
chao.xia@tongji.edu.cn

<sup>1</sup> Shanghai Key Lab of Vehicle Aerodynamics and Vehicle Thermal Management Systems, Shanghai 201804, China

<sup>2</sup> Shanghai Automotive Wind Tunnel Center, Tongji University, Shanghai 201804, China

<sup>3</sup> Beijing Aeronautical Science & Technology Research Institute, Beijing 102211, China

wake of a HST has been found to be related to the periodic unsteadiness and oscillation behaviour of this vortex pair [3–5]. The safety of passengers waiting on platforms, platform furniture, trackside workers, and loadings on nearby structures can be deteriorated by the high slipstream velocity [6–10]. Furthermore, the fluctuant pressure on the tail train caused by this periodic unsteadiness in the wake has effects on the drag and stability of a HST [4]. Hence, comprehensive understanding of the unsteady wake behind a HST is of great significance.

Weise et al. [11] found two typical flow patterns via a wind tunnel test: separation bubble and vortex shedding. These occur alternately in the near wake of a train depending on the train rear shape. Werning et al. [12] numerically identified lateral oscillation of the streamwise vortex pair ( $St = f D/U = 0.14$ ,  $D$  is the hydraulic diameter) using an unsteady Reynolds-averaged Navier-Stokes (URANS) approach, which conformed to the characteristic frequency of the side force. Two typical dominant flow patterns, i.e., vortex shedding and the bending of the counter-rotating streamwise vortices, were recognized by a delayed detached eddy simulation (DDES) combined with decomposition methods (Proper Orthogonal Decomposition, POD and Dynamic Mode Decomposition, DMD) in the wake of a HST by Muld et al. [13]. Utilizing the Lattice Boltzmann Method, Pii et al. [14] detected vortex shedding ( $St = f W/U = 0.15\text{--}0.18$ ,  $W$  is the train width), which developed from the bogie section due to interaction with the bogies. The transient pressure and velocity in the near wake show lateral fluctuations. However, their inherent connection to the wake dynamics has not yet been fully understood. Östh et al. [15] performed cluster-based reduced-order modelling analysis of the wake of a simplified HST, and two groups of clusters were associated with streamwise vortices and vortex shedding. Bell et al. [3] proposed that the wake dynamics of a HST is characterized by sinusoidal, antisymmetric motion of the counter-rotating streamwise vortex pair, which could be triggered by periodic vortex shedding from the side of the train. Wang et al. [16] investigated the effect of bogies on slipstream and wake. They found stronger spanwise oscillation in the presence of bogies and attribute this oscillation to the amplification of a natural instability of the pair of counter-rotating streamwise vortices rather than alternating vortex shedding from the bogie section. Xia et al. [5, 17] studied ground effects on the unsteady wake and slipstream of a HST with the improved delayed detached eddy simulation (IDDES). They elucidated the inherent connection between the instantaneous streamwise vortex pair and the slipstream peak and suggested that the wake oscillates more violently under the stationary ground conditions compared with moving ground conditions.

Recently, based on wind tunnel experiments, Xia et al. [18] deduced that the unsteady wake topology of a HST is dominated by an alternating half-loop vortex shedding, which is akin to the flow topology behind the finite wall-mounted rectangular cylinder proposed by Bourgeois et al. [19]. This vortex structure is inherently distinct from the sinusoidal, synchronous and antisymmetric motion of the pair of counter-rotating streamwise vortices in the wake of a HST depicted by Bell et al. [3] and Wang et al. [16]. However, the origin of the vortex shedding has not yet been confirmed due to the complexity of the underbody configuration (the support pillars, the bogies and the rail) in the wind tunnel test. The impact of bogie sections on the half-loop vortex shedding of a HST has not been properly investigated in the present literature. This effect is expected to explain the origin of the vortex shedding and its influence on the wake dynamics of a HST. Moreover, the instantaneous and spatial evolution of the unsteady half-loop vortex structures have not been clearly depicted in previous studies.

In general, CFD can overcome some limitations of practical wind tunnel tests. For instance, wind tunnel interference (blockage, support pillars and ground boundary layer, etc.) can be easily removed. Moreover, it is more convenient to change the configuration of the physical

model utilizing CFD. Additionally, CFD offers much more 3D flow information, which contributes to the understanding of the mechanisms of the issues concerned [20]. Time-dependent numerical simulations such as PANS, DES and LES have been viable tools for investigating HST unsteady aerodynamics due to their increasing availability and accuracy [21–23]. The main intention of the present work is to further confirm the origin of the vortex shedding and its interaction with the dynamics of the streamwise vortex pair by numerically studying the impact of underbody configurations, e.g., with and without the bogie sections, on the wake dynamics of a HST using IDDES. The focus is placed on the spatio-temporal evolution of the unsteady wake. The POD technique was utilized to extract the dominant coherent structure and reveal the wake dynamics.

## 2 Method

### 2.1 Physical model

A 1/50th scale train model (China Railway High-Speed 3, CRH3) is chosen to carry out this research with  $L/W$  (slenderness ratio) of 15.7 where  $L$  and  $W$  ( $W$  is 0.065 m) denote the length and width of the train model, respectively. The three-dimensional size of the CRH3 model is  $1.0 W$  (Width)  $\times 1.1 W$  (Height)  $\times 15.7 W$  (Length). Two different underbody configurations were considered in this paper: One is a simplified train model (STM) with a flat underbody, as shown in Fig. 1(a). The other is a complex train model (CTM) with two coaches, two cowcatchers and four sets of bogies, as shown in Fig. 1(b).

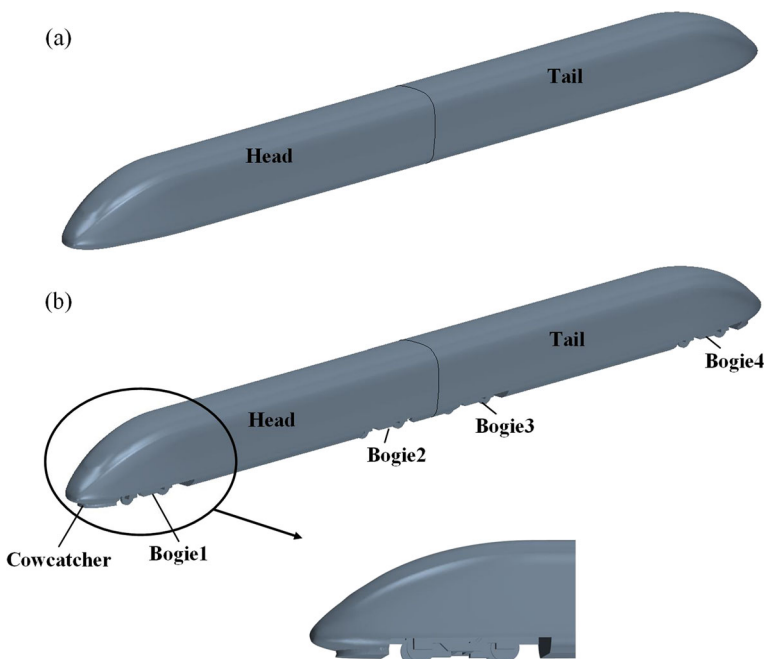


Fig. 1 1/50th scale HST model with two coaches: (a) STM, (b) CTM

## 2.2 Computational domain and boundary conditions

As shown in Fig. 2, the computational domain is  $5.2 W$  (width)  $\times 5 W$  (height)  $\times 54 W$  (length). The distance between the inlet and the nose tip of the head train is  $6.0 W$ , while the distance from the tail nose tip to the outlet is  $32 W$ . These dimensions give a blockage ratio of 2.3%. The definition of the coordinate system  $(x, y, z)$  is shown in Fig. 2 with the origin lying in the spanwise middle of the ground below the tip end of the tail train. The boundary conditions of the domain are specified as follows: velocity inlet for inlet, pressure outlet for outlet, moving wall condition with the inlet velocity for the floor, non-slip wall condition for the train body and symmetry for the rest of the boundaries. The Reynolds number ( $Re$ ), based on  $U_\infty = 30$  m/s and  $H$ , is  $1.3 \times 10^5$ . All the above mentioned setups are the same for the two underbody configurations.

It should be acknowledged that some limitations exist in the present simulation, e.g., the reduced slenderness ratio  $L/W$  and the reduced  $Re$  of the train model (the  $L/W$  and  $Re$  of a full-scale train with 8 coaches travelling at 300 km/h are 62.8 and  $1.7 \times 10^7$ , respectively). Investigations of the quantitative effects of these factors on the wake dynamics are still on going. However, our experimental results at the same  $L/W$  and  $Re$  [18] have proved to be in reasonably agreement with previous investigations that use different train lengths and higher  $Re$  [3, 5, 14, 17]. This suggests that the results of this work are representative of the wake dynamics of a HST, as shown in § 3.

## 2.3 Numerical setup

The time-dependent IDDES (based on an SST  $k-\omega$  model) used in this paper is a hybrid RANS-LES model, which combines the advantages of the DDES and the wall-modelled large eddy simulation (WMLES) [24]. The DDES provides shielding against grid-induced separation (GIS) caused by grid refinement beyond the limit of the modelled stress depletion (MSD) [25]. The WMLES model is designed to reduce the Reynolds number dependency and to allow the LES simulation of wall boundary layers at much higher Reynolds numbers than in standard LES models [24, 26]. In the present IDDES, a new sub-grid length-scale is defined in Eq. (1) including explicit wall-distance dependence, which is different from the traditional LES and DES involving only the grid spacing. The primary effect of Eq. (1) is to reduce  $\Delta$  and to give it a fairly steep variation leading to a similar trend in the eddy viscosity, which is likely to de-stabilize the flow [24].

$$\Delta = \min\{\max[C_w d_w, C_w h_{wn}], h_{max}\} \quad (1)$$

In Eq. (1),  $d_w$  is the distance to the wall,  $h_{wn}$  is the grid step in the wall-normal direction, and  $C_w$  is an empirical constant that is equal to 0.15 based on a wall-resolved LES of channel flow [24].  $h_{max}$  in Eq. (1) is defined as the largest local grid spacing, as shown in Eq. (2). The

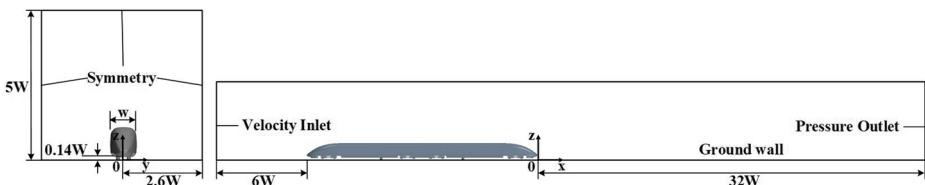


Fig. 2 Computational domain and boundary conditions



complete formulations for the IDDES are not shown here for simplicity. Readers may refer to Shur et al. [24] for further details.

$$h_{max} = \mathbf{max}\{h_x, h_y, h_z\} \quad (2)$$

A segregated incompressible finite-volume solver was employed in STAR-CCM+ 11.06.010. The convective terms of the momentum equations were discretized by a hybrid numerical scheme [27] that switches between a Bounded Central Differencing Scheme (BCDS) where LES is active and a second order upwind scheme where the RANS mode is active. The scheme for the turbulent quantities was a second order upwind. The second order accuracy was used for temporal discretization. The simulation was initialized by a steady RANS (based on the SST  $k-\omega$  model) result to save computational time and then transformed to IDDES. The sampling was commenced after  $208 t^*$  ( $t^* = H/U_\infty$ ) when no significant differences of the mean and rms values of the aerodynamic forces were found for two consequent time sequences. The averaging time was  $416 t^*$ , which corresponds to the time for 30 passages of the train at free stream velocity.

The topology of the computational grid is trimmer, which contains prism layers at the wall boundaries and a perfect hexahedral grid in the rest of the domain. The prism layers are connected to the hexahedral grids by trimming. A sensitivity study is performed on four different grids with different numbers of cells for the complex model: coarse, medium, fine and very fine grids consisting of 5.7 million, 9.7 million, 13.6 million and 18.4 million cells, respectively. The fine grids section distribution is shown in Fig. 3. Table 1 presents the maximum spatial resolutions of the model surface-cells expressed in the wall units where  $n$  is the distance between the first node and the train surface in the wall normal direction,  $\Delta s$  is the cell width in the spanwise direction,  $\Delta l$  is the cell width in the streamwise direction, and  $u^*$  is the friction velocity. The time steps were  $0.008 t^*$  and  $0.004 t^*$  for the first three sets of grids and very fine grids, respectively. Thus, only in approximately 1% of the grids did the Courant number (Co) exceeded 1, and several studies [16, 28, 29] have shown that this minor infringement on the Co requirement has little effect on the flow field.

## 2.4 Numerical validation

The numerical simulations in this work were validated by an experiment conducted in a closed-loop low-speed wind tunnel including aerodynamic forces, pressure measurement and PIV. The dimension of the test section is 2 m (L)  $\times$  0.555 m (W)  $\times$  0.333 m (H). The

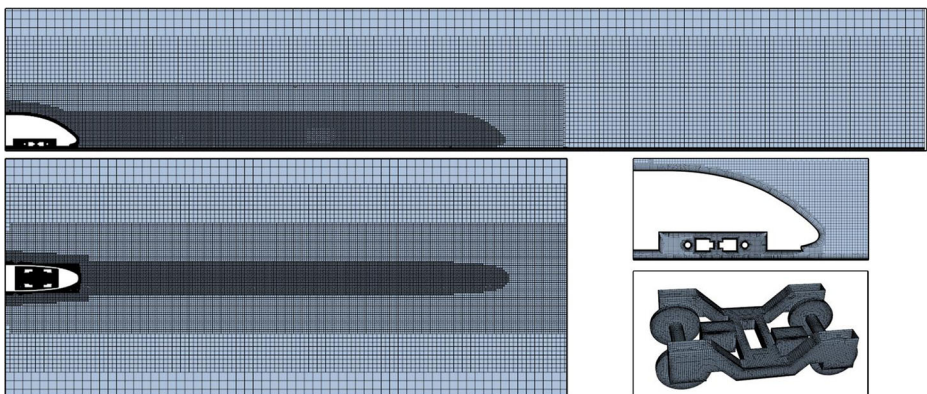


Fig. 3 Fine grid distribution around a HST

**Table 1** Spatial resolutions for coarse, medium, fine and very fine grids

Grids	$y^+ = nu^*/\nu$	$z^+ = \Delta su^*/\nu$	$x^+ = \Delta lu^*/\nu$	Total number
Coarse	30	70	70	5.7 million
Medium	5	70	70	9.7 million
Fine	1	70	70	13.6 million
Very Fine	1	50	50	18.4 million

longitudinal turbulent intensity at the exit of the contraction section was less than 0.5%. The floor is stationary, i.e., no relative motion between the train model and the floor during the wind tunnel test. Hence, the IDDES case used for numerical validation also adopts a stationary floor. The tested train model has the same scale,  $L/W$ , as well as other detailed features as the numerical model (including four cylindrical struts for comparison with the wind tunnel test). The other experimental details can be found in [18].

### 2.4.1 Aerodynamic Forces

The time-averaged drag force comparison between wind tunnel test and numerical simulation is shown in Table 2. The force coefficient is defined as follows:

$$C_D = \frac{F_x}{\frac{1}{2} \rho U_\infty^2 A_x} \quad (3)$$

where  $F_x$  is the drag force,  $\rho$  is the density of air,  $U_\infty$  is the inlet velocity, and  $A_x$  is the projected area in the  $x$  direction. The  $C_D$  results show minor differences among all sets of grids. Compared to experimental results, the deviation of  $C_D$  is 10.1%, 8.9%, 3.9% and 2.5% for coarse, medium, fine and very fine grids, respectively. Overall, the deviation of  $C_D$  results in IDDES for the four sets of grids deviates by less than 10.1% from the experimental results.

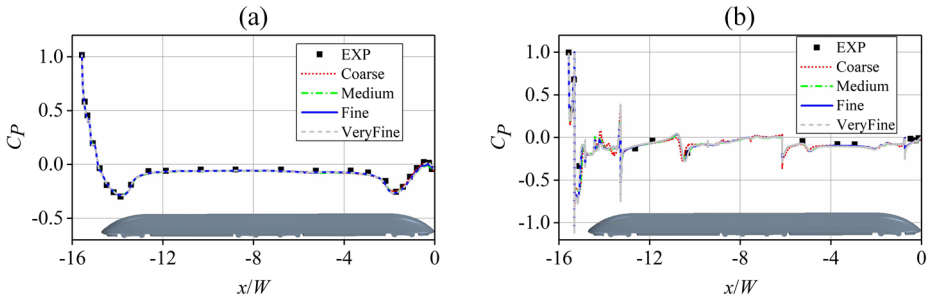
### 2.4.2 Pressure distribution

Figure 4 presents the pressure coefficient ( $C_p$ ) distribution along the longitudinal centreline of the head and tail train over the upper and lower surface for both IDDES and the wind tunnel test.  $C_p$  is defined in Eq. (4) where  $P$  is the time-averaged surface pressure and  $P_\infty$  is the static pressure of the freestream.

$$C_p = \frac{P - P_\infty}{\frac{1}{2} \rho U_\infty^2} \quad (4)$$

**Table 2** Time-averaged  $C_D$  comparison between IDDES and experiments

Force coefficients	IDDES				EXP
	Coarse	Medium	Fine	Very Fine	
$C_D$	0.421	0.416	0.397	0.392	0.382



**Fig. 4** Comparison of time-averaged  $C_p$  of the longitudinal centreline between IDDES and experiment: (a) the upper surface, (b) the lower surface

As shown in Fig. 4, the IDDES results using the medium, fine and very fine grids correspond well with each other for both upper and lower surfaces. However, the  $C_p$  distribution using coarse grids has obvious deviations from the other three sets of grids. This is especially true in the lower surface and near wake. In general, the IDDES with fine grids is in good agreement with the experimental results except at the positions behind the bogie sections and near the wake. The grid sensitivity test indicates that the resolution of the fine grids is adequate for this work. Thus, the following discussions are all based on the results using fine grids.

**2.4.3 Velocity distribution**

Figure 5 compares the velocity and velocity fluctuation distribution between IDDES and PIV data in the  $(x, y)$  plane at  $z/W = 0.54$  for different  $x$ -direction positions ( $x/W = 0.8, x/W = 1.5, x/W = 1.5, x/W = 3.0, x/W = 4.6$ )

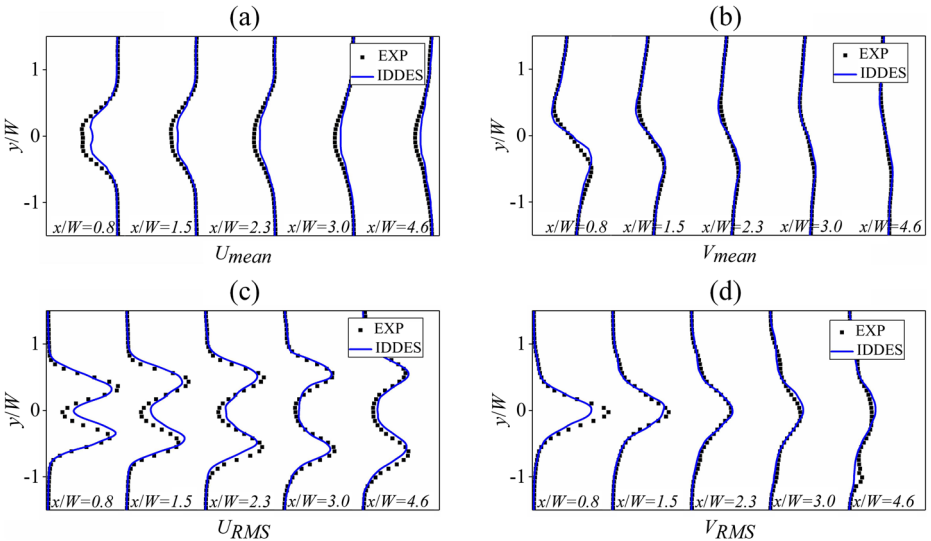


**Fig. 5** Comparison of IDDES and PIV data in the  $(x, y)$  plane at  $z/W = 0.54$  for different  $x$ -direction positions ( $x/W = 0.8, x/W = 1.5, x/W = 2.3, x/W = 3.0$  and  $x/W = 4.6$ ): (a) time-averaged  $x$ -direction velocity  $U_{mean}$ , (b) time-averaged  $y$ -direction velocity  $V_{mean}$ , (c)  $x$ -direction velocity fluctuation  $U_{RMS}$ , (d)  $y$ -direction velocity fluctuation  $V_{RMS}$

$W=2.3$ ,  $x/W=3.0$  and  $x/W=4.6$ ). As shown in Fig. 5a and b, the time-averaged velocity profiles obtained from IDDES using the fine grid are in good agreement with the PIV data except for the minor difference near the wake, which could be attributed to the different boundary layer thickness between IDDES and PIV data. Similarly, the overall velocity fluctuation profile of IDDES corresponds well with the PIV results apart from some obvious deviations in the peak near the wake, as shown in Fig. 5c and d. This deviation is not unexpected in view of the intensive unsteadiness in the near wake.

In conclusion, the overall agreement in the drag force, pressure distributions and velocity profiles indicates that IDDES using the fine grid can be used to study the wake dynamics of a HST.

## 2.5 Proper orthogonal decomposition

To investigate the spatial-temporal evolution of the unsteady wake, we use proper orthogonal decomposition (POD) to extract the most energetic coherent structures in the wake of a HST due to its significant reduction in the required computation and memory resources. The snapshot POD method proposed by Sirovich [30] has been widely used to extract POD modes from high-dimensional fluid flow data [31–33] and is presently employed for decomposing the velocity data obtained from IDDES. Briefly, the first step is to calculate the mean velocity field,  $U(\xi)$ , of the given flow field,  $U(\xi, t)$ , which is then removed from each of the instantaneous snapshots. The rest of the analysis works on the fluctuating components of the velocity:

$$x(t) = U(\xi, t) - U(\xi) \in \mathbb{R}^n, \quad t = t_1, t_2, \dots, t_m. \quad (5)$$

Here,  $x(t)$  is taken to be the fluctuating component of the velocity vector with the time-averaged value  $U(\xi)$  removed. The objective of the POD analysis is to find the optimal basis vectors that can best represent the given data. The solution to this problem is to find the eigenvectors  $\psi_j$  and eigenvalues  $\lambda_j$  from

$$\mathbf{R}\psi_j = \lambda_j\psi_j, \quad \phi_j \in \mathbb{R}^n, \quad \lambda_1 \geq \dots \geq \lambda_n \geq 0, \quad (6)$$

where  $\mathbf{R}$  is the correlation matrix of the vector  $x(t)$

$$\mathbf{R} = \sum_{i=1}^m x^T(t_i)x(t_i) = \mathbf{X}^T\mathbf{X} \in \mathbb{R}^{n \times n}, \quad (7)$$

where the matrix  $\mathbf{X}$  represents the  $m$  snapshots of data being stacked into the matrix form given by

$$\mathbf{X} = [x(t_1) \ x(t_2) \ \dots \ x(t_m)] \in \mathbb{R}^{n \times m}. \quad (8)$$

With the eigenvectors  $\psi_j$  of the above smaller eigenvalue problem determined, the POD modes can be recovered through

$$\phi_j = \mathbf{X}\psi_j \frac{1}{\sqrt{\lambda_j}} \in \mathbb{R}^n, \quad j = 1, 2, \dots, m. \quad (9)$$

When the velocity vector is used for  $x(t)$ , the eigenvalues  $\lambda_j$  correspond to the turbulence kinetic energy captured by the respective POD modes. We can use the eigenvalues to

determine the number of modes needed to represent the fluctuations in the flow field data. Generally, we retain only  $r$  number of modes to express the flow such that

$$\sum_{i=1}^r \lambda_j / \sum_{i=1}^m \lambda_j \approx 1. \quad (10)$$

With the determination of the important POD modes, we can represent the flow field solely in terms of a finite or truncated series,

$$U(\xi, t) \approx U(\xi) + \sum_{j=1}^r a_j(t) \phi_j(\xi) \quad (11)$$

in an optimal manner effectively reducing the high-dimensional ( $n$ ) flow field to a representation with only  $r$  modes. The temporal coefficients are determined by

$$a_j(t) = \langle U(\xi, t) - U(\xi), \phi_j(\xi) \rangle = \langle x(t), \phi_j \rangle. \quad (12)$$

The current POD code has been successfully applied in our previous studies and fully verified [18, 34]. The sampling rate in this work was 2000 Hz. A total of 1000 snapshots were sampled for the POD analysis in each plane section, which was considered to be adequate for the present analysis.

## 3 Results

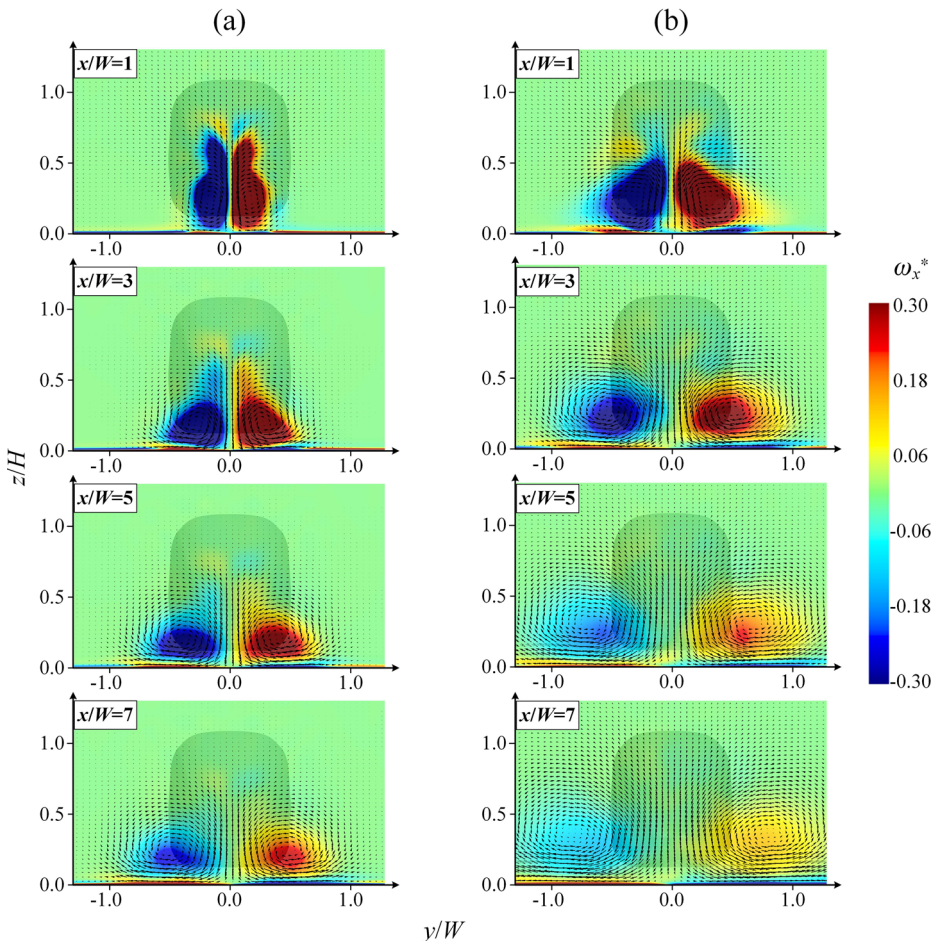
### 3.1 Time-averaged wake flow

The time-averaged streamwise vorticity contours,  $\omega_x^*$ , and velocity vectors,  $(v, w)$ , in the  $(y, z)$  plane at  $x/W = 1, 3, 5$  and  $7$  in the wake of the STM and the CTM are shown in Fig. 6a and b, respectively. A superscript “\*” denotes normalization by maximum  $\omega_x$ ,  $\omega_z$  or  $U_\infty$  in this paper. It should be noted that a dominating pair of counter-rotating streamwise vortices exist for both underbody configurations and are well established in the previous literature [1–5, 17, 35, 36]. The vortex pair moves outwards as it is advected downstream. The vortex pair is induced by itself and by interaction with the image pair, to initially move towards the ground and then away from each other [2, 4]. Some level of flattening of the cores can be noted when the pair approaches the ground [5, 17]. However, the difference in the time-averaged streamwise vortex pair between the two underbody configurations (STM and CTM) can be easily observed in Fig. 6. The size of the streamwise vortices and the space between the two vortex cores are both larger for the CTM relative to those for the STM, which can be attributed to the interaction between the streamwise vortices and vortex shedding originating from the side of the bogie sections. On the other side, the streamwise vortex in the CTM case presents more rapid vorticity diffusion when moving downstream due to the severe swing of the streamwise vortices compared to the STM case, as shown at  $x/W = 3, 5$  and  $7$ . In addition, the higher cores of the streamwise vortices for the CTM case can be noted at  $x/W = 5$  and  $7$ . In conclusion, in terms of the time-averaged flow, the wake is closely related to the underbody configurations.

### 3.2 Instantaneous wake flow

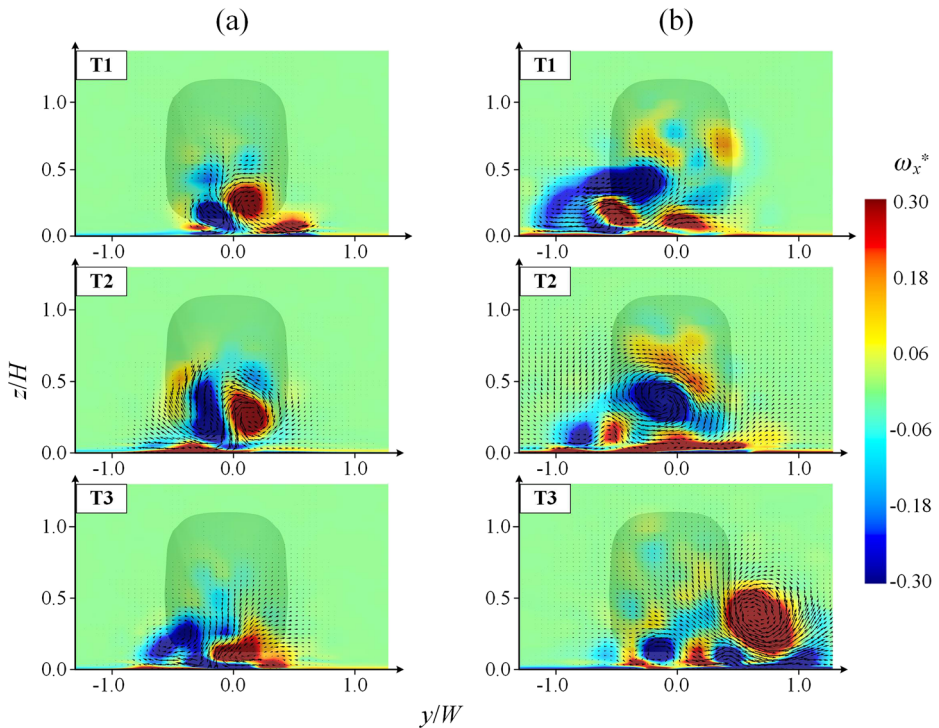
#### 3.2.1 Spanwise wake dynamics

Figure 7a and b present three typical instantaneous flow structures in the  $(y, z)$  plane at  $x/W=3$  for the STM and the CTM, respectively. Both the streamwise vorticity contour,  $\omega_x^*$ , and velocity vector,  $(v, w)$ , are shown. For both underbody configurations, the two vortices characterized by the most highly concentrated vorticity are exactly the well-known pair of streamwise vortices [17, 18]. In addition, near each streamwise vortex, some relatively strong vorticity concentrations are observed, the sign of which is opposite to that of the streamwise vortices. The streamwise vortex pair swings in the spanwise and vertical direction for both underbody configurations. However, the differences in the spanwise wake dynamics between the two underbody configurations are evident. Compared to the STM, a more intensive swing of the vortex pair can be noted for the CTM, as shown in Fig. 7, which leads to a wider near wake. Moreover, for the STM, each of the



**Fig. 6** Time-averaged vorticity contours,  $\omega_x^*$ , and velocity vectors,  $(v, w)$ , in the  $(y, z)$  plane: (a) STM, (b) CTM





**Fig. 7** Instantaneous streamwise vorticity contour,  $\omega_x^*$ , and velocity vector,  $(v, w)$ , (three random snapshots) in the  $(y, z)$  plane at  $x/W=3$ : (a) STM, (b) CTM

vortices in the vortex pair are coupled with each other and appear simultaneously, as shown in Fig. 7a. On the contrary, the large-scale streamwise vortices with the opposite sense of rotation appear alternately in the wake of the CTM implying that the vortex structures are shed alternately from the left or right side of the tail, which can be explicitly observed in the 3D flow structures, as shown in Fig. 9b. This instantaneous feature coincides with the full-scale numerical results performed by [36] and our previous numerical results at 1/8th scale [5, 17].

### 3.2.2 Streamwise wake dynamics

Three typical instantaneous snapshots in the  $(x, y)$  plane at  $z/W=0.12$  are shown in Fig. 8 to illustrate the streamwise wake dynamics. Both the vertical vorticity contour,  $\omega_z^*$ , and velocity vector,  $(u, v)$  are shown.

For the STM, the vortex pairs are well aligned suggesting their simultaneous appearance and transformation, as shown in Fig. 8a. However, the arrangement of vortices in the CTM appears to be different and complex. The spanwise range of the wake for the CTM is larger than that of the STM due to the more intense oscillation of the vortices. By comparing the three snapshots of the CTM (Fig. 8b), it can be clearly noted that the distribution of positive and negative vorticity is staggered, i.e., large-scale vortices are shed from the left or right side of the tail alternately, which is similar to the classical Von Karman vortex shedding behind a two-dimensional circular or square cylinder.



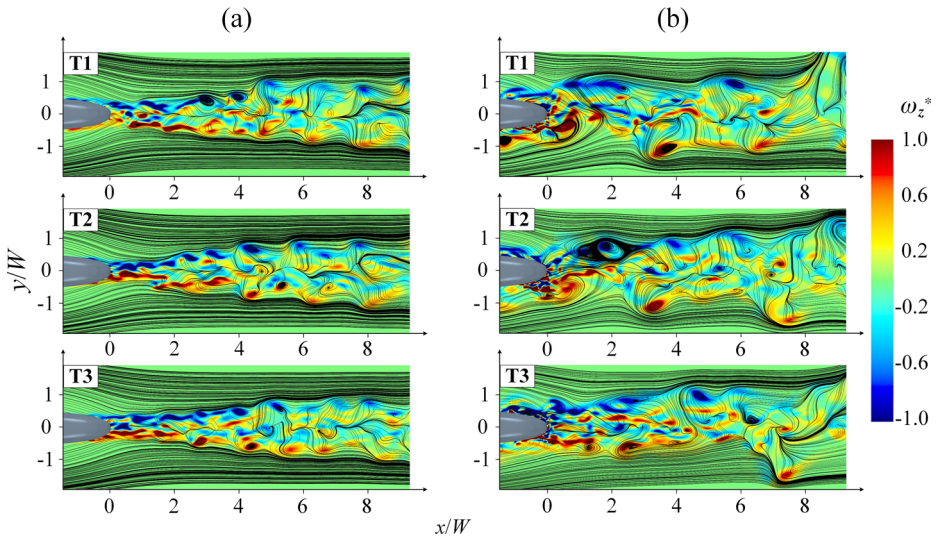


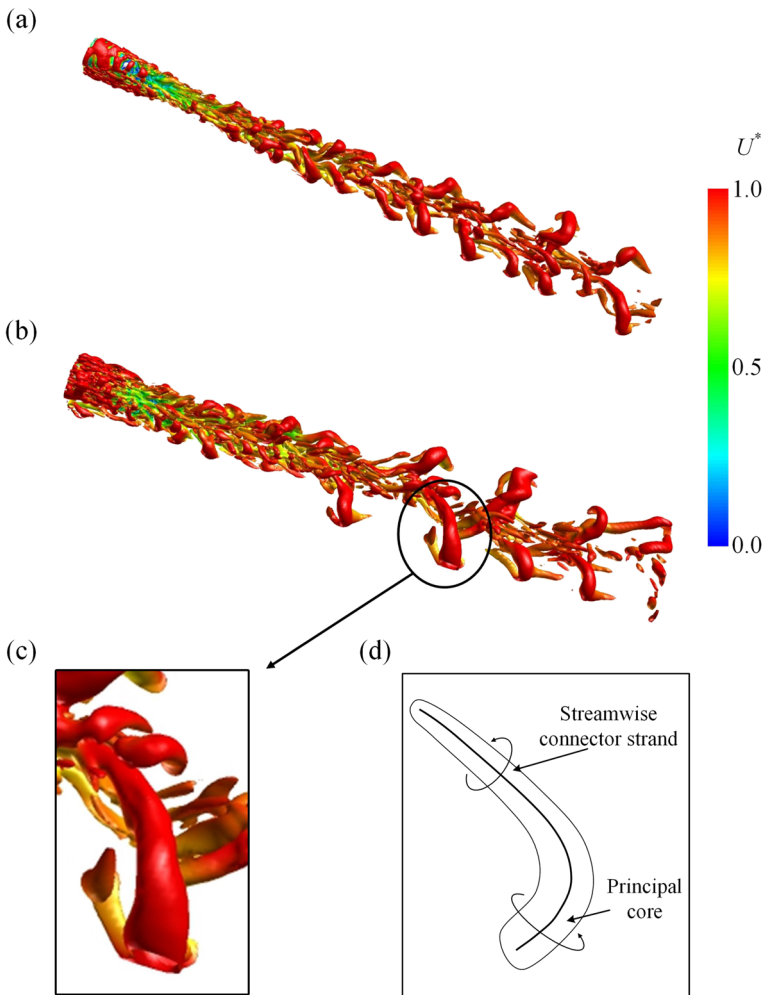
**Fig. 8** Instantaneous vertical vorticity contour,  $\omega_z^*$ , and velocity vector,  $(u, v)$ , (three random snapshots) in the  $(x, y)$  plane at  $z/W = 0.12$ : (a) STM, (b) CTM

### 3.2.3 Three-dimensional flow structures

In this part, the three-dimensional wake topology is identified by means of the  $Q$ -criterion [37]. The  $Q$ -criterion is positive at a vortex core since this indicates that the anti-symmetric part is larger than the symmetric part, i.e., the rotation is larger than the strain. In general, vortex cores can be identified in the wake flow where the  $Q$ -criterion is large.

Figure 9a and b show the typical snapshots of the iso-surface defined by  $Q$ -criterion = 10000 for the STM and the CTM, respectively, which are coloured with the streamwise velocity,  $U^*$ . For both underbody configurations, large-scale streamwise vortex shedding dominates the wake with the vortex leg attached to the ground, as shown in Fig. 9. Moreover, the topology of each vortex, as shown in Fig. 9c, is similar to the half-loop structure observed in the wake of a finite-square cylinder [19, 38–40], as sketched in Fig. 9d. The half-loop vortex structure has a streamwise connector strand which is the underlying cause of the streamwise vorticity in the  $(y, z)$  plane (Figs. 6 and 7) and a leading principal core which is nearly vertical at the ground plate contributing to the vertical vorticity in the  $(x, y)$  plane (Fig. 8). The streamwise connector strand and principal core can keep their geometrical shape and orientation during the vortex shedding period (not shown here). This half-loop structure corresponds well with our previous conjecture based on the flow visualization and PIV results [18]. In addition, small-scale vortices are generated alongside the large-scale vortices due to the instability of high shearing among large-scale vortices and the ground caused by vortex stretching, tilting and cutting [17].

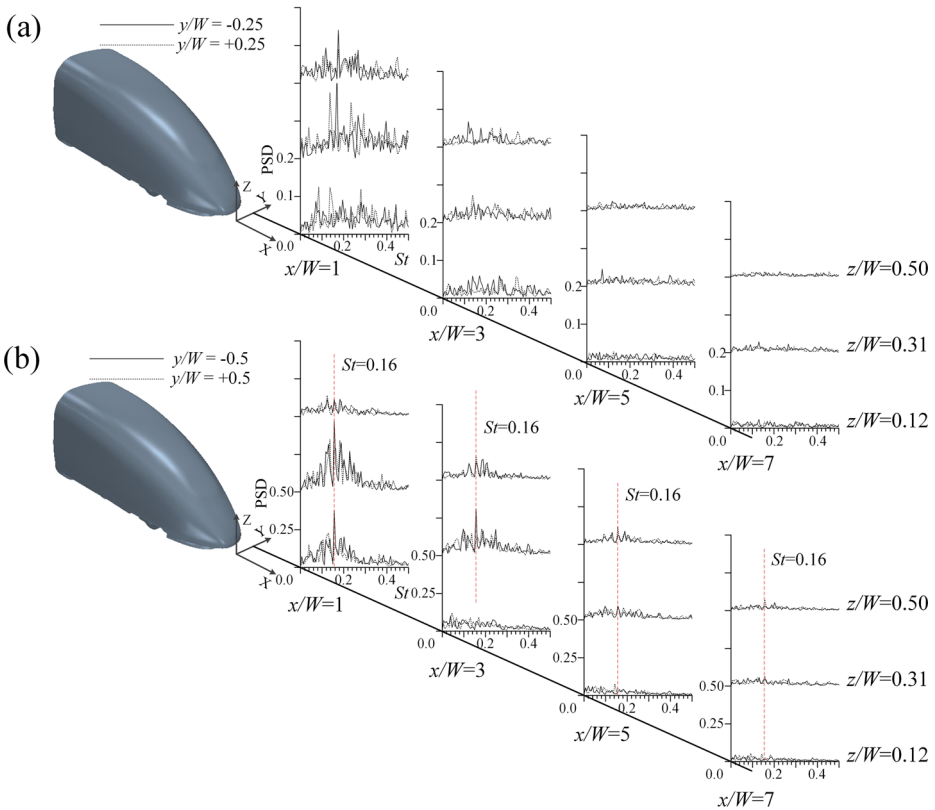
The difference between the two underbody configurations in the wake topology can be noted in Fig. 9a and b; however, the wake flow is quite complex. For the STM, shown in Fig. 9a, each of the half-loop structures shed simultaneously, and the size of the vortices is smaller than that of the CTM, which is consistent with the simultaneous vortex couple in the plane section of the STM's wake, as shown in Figs. 7a and 8a. This simultaneous vortex shedding can also be observed in the numerical study performed by [41] with a 1/8th scale simplified train model (without bogies). However, for the CTM, the staggered arranged half-loop



**Fig. 9** (a) Iso-surface of  $Q$ -criterion = 10000 (three random snapshots) coloured by the streamwise velocity,  $U^*$ , of the STM, (b) iso-surface of  $Q$ -criterion = 10000 (three random snapshots) coloured by the streamwise velocity,  $U$ , of the CTM, (c) the enlarged view of a typical vortex in the wake, (d) schematic of the half-loop structure

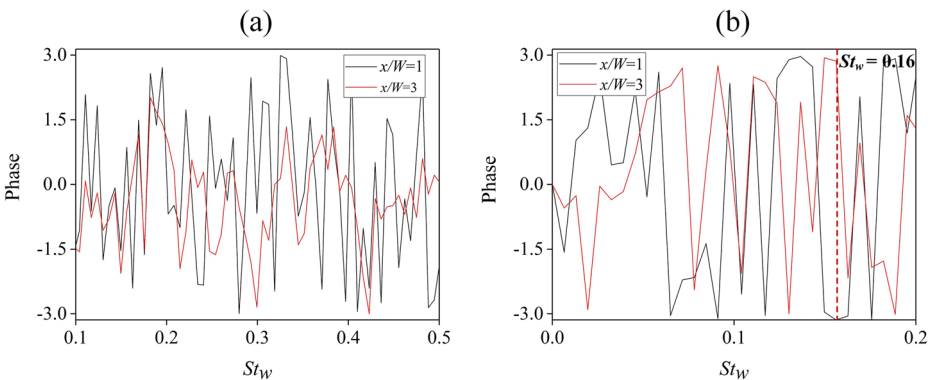
structures are shed alternately from both sides of the tail train and have gotten larger as they move downstream. This is also confirmed by the phase shift near  $\pi$ , i.e., out of phase, at  $St_w = 0.16$  for the streamwise velocity,  $u_x$ , signals at  $y/W = \pm 0.5$ , and  $z/W = 0.12$  (Fig. 11b). These staggered arranged half-loop structures can also be detected in the numerical results at higher Reynolds numbers with the complex train models [17, 26, 35, 42], which indicates that the present Reynolds number has little effect on the unsteady wake topology of a HST.

Figure 10a and b present the power spectrum density (PSD) of the instantaneous streamwise velocity,  $u_x$ , measured at different positions for the STM and the CTM. The positions distribute at  $x/W = 1, 3, 5$  and  $7$ ,  $z/W = 0.12, 0.31$  and  $0.50$ , and  $y/W = \pm 0.25$  for the STM but at  $y/W = \pm 0.5$  for the CTM, since the oscillation region in the wake of the STM is narrower. This shows that the dominating PSD value peak is at the frequency  $St_w = 0.16$  at



**Fig. 10** PSD of the streamwise velocity,  $u_x$ , in the wake at  $x/W = 1, 3, 5$  and  $7, z/W = 0.12, 0.31$  and  $0.50$ : (a) STM ( $y/W = \pm 0.25$ ), (b) CTM ( $y/W = \pm 0.5$ )

most monitor points in the CTM case. The PSD value is higher at  $z/W = 0.31$  than for the other two horizontal planes, and the PSD value decreases further into the wake due to the energy dissipation of the vortex structures. The presently observed dominant frequency is in agreement with the LBM results for a full-scale train with 11 cars that was performed by



**Fig. 11** Cross spectrum (phase shift) of the streamwise velocity,  $u_x$ , at  $y/W = \pm 0.25$  ( $x/W = 1$  and  $3, z/W = 0.12$ ): (a) STM, (b) CTM ( $y/W = \pm 0.5$ )

[14], who identified vortex shedding at  $St_w = 0.15\sim 0.18$  for a Re of  $2.3 \times 10^7$ . However, the PSD result presents differently in the STM case compared with the CTM case. The PSD value is smaller than that of the CTM, and there is not a single dominating peak but multiple peaks ( $St_w = 0.12 \sim 0.16$  and  $0.39$ ).

Figure 11a and b show the phase shift between the streamwise velocities,  $u_x$ , signals monitored simultaneously at  $y/W = \pm 0.25$  ( $x/W = 1$  and  $3$ ,  $z/W = 0.12$ ) for the STM and for the CTM ( $y/W = \pm 0.5$ ), respectively. An approximate  $\pi$  phase shift at  $St_w = 0.16$  can be detected for the CTM, as shown in Fig. 11b, which confirms the periodic and alternating vortex structures in the wake of the CTM. However, for the STM, as shown in Fig. 11a, the phase shift is approximately zero (around the range  $[-1.5, 1.5]$ ) at  $St_w = 0.12\sim 0.16$  and  $0.39$ , indicating the periodic and synchronous vortex structures behind the STM.

### 3.3 Proper orthogonal decomposition (POD) analysis

To further understand the differences in the wake dynamics between the two underbody configurations, the snapshot POD method, as described in section 2.5, was used to extract the coherent structures of the wake flow field. Then, the flow reconstruction based on the mean flow and POD modes was applied to investigate which flow structure is associated with which mode.

Figure 12 shows the turbulence Kinetic Energy (TKE) contribution of the first hundred POD modes for both underbody configurations in the  $(y, z)$  plane at  $x/W = 3$  and  $(x, y)$  planes at  $z/W = 0.12$ . The TKE contribution of each mode, and the accumulation of the first hundred modes, are presented in Fig. 12a and b, respectively.

#### 3.3.1 Spanwise wake dynamics

Figure 13a and b visualize the first four POD modes in the  $(y, z)$  plane at  $x/W = 3$  for the STM and the CTM, respectively, represented by the streamwise vorticity contours  $\omega_x^*$ , and the velocity vectors,  $(v, w)$ . The thresholds are chosen to give a good visual representation of the mode, and the thresholds are the same for the different modes in both cases. The POD modes data are calculated by Eq. (6) and (9), which are the optimal basis vectors that can best represent the given flow field data.

As shown in Fig. 12 for the STM, the first four modes contribute 50.4% of the total TKE energy in the  $(y, z)$  plane at  $x/W = 3$  and are of relatively higher significance in the described

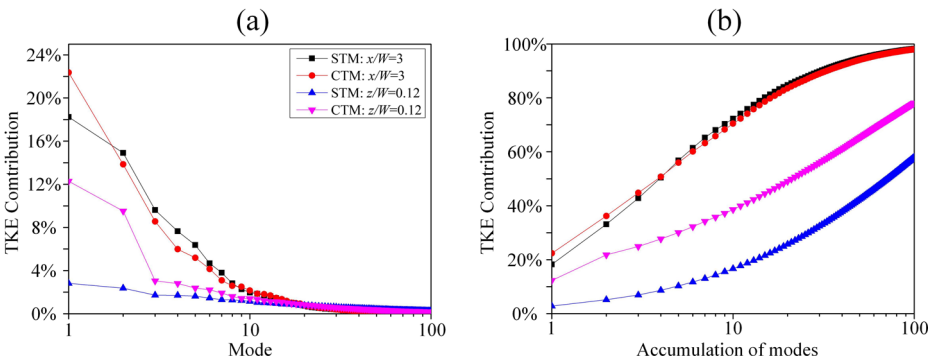
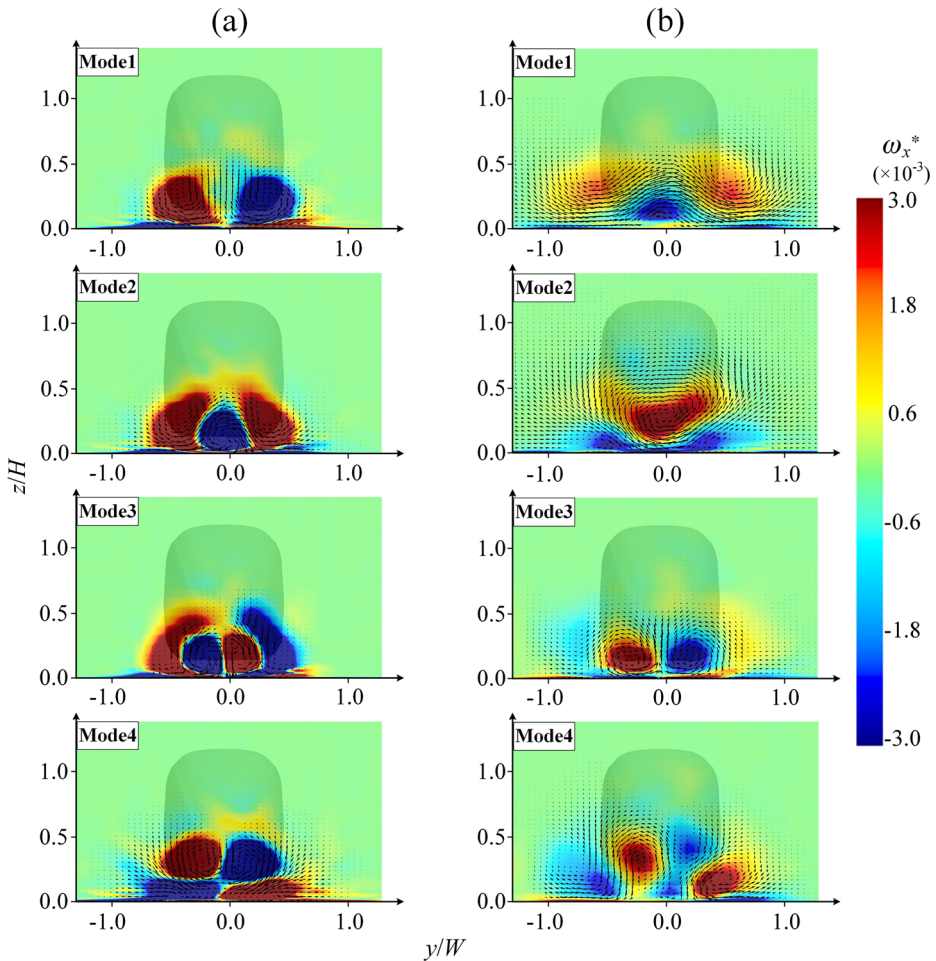


Fig. 12 Turbulence Kinetic Energy contribution: (a) each mode, (b) accumulation of the first hundred modes



**Fig. 13** The first four modes in the  $(y, z)$  plane at  $x/W=3$ : (a) STM, (b) CTM

wake. Particularly, the first mode is clearly dominant, with a significant contribution to the TKE of up to 18.2%. Its magnitude decreases to 14.9%, 9.6% and 7.6% corresponding to mode 2, mode 3 and mode 4, respectively. It is evident from the contour of the streamwise vorticity,  $\omega_x$ , that mode 1 contains two counter-rotating vortices, as shown in Fig. 13a. Mode 2 describes an oscillating swing of the two counter-rotating vortices along the spanwise direction. Mode 3 and mode 4 seem to be connected with the horizontal and vertical motion of the vortex pair.

For the CTM, the first four modes contribute 50.7% of the total TKE energy in the  $(y, z)$  plane at  $x/W=3$ , which also shows relatively higher significance in the near wake described in Fig. 12. Mode 1 occupies 22.4% of the total TKE, which is 4.2% higher than that of the STM. Mode 2, mode 3 and mode 4 show a significant contribution with 13.8%, 8.6% and 6%, respectively. Higher modes have lower and lower contributions.

As shown in Fig. 13b, the modes of the CTM in the  $(y, z)$  plane at  $x/W=3$  exhibit distinct characteristics from those for the STM. Mode 1 is characterized by two large-scale streamwise vortices with a small-scale streamwise vortex between them. This feature is similar to mode 2

of the STM. Mode 2 of the CTM presents a dominant streamwise vortex with a strong induced sweep flow across the centre line. Mode 3 presents a couple of symmetrical small-scale streamwise vortices located in the low part of the wake. Mode 4 seems to be connected with the vortex oscillation in the diagonal direction.

The differences between the two underbody configurations are also studied for the temporal coefficients of the modes. This is done by looking at the Fourier transform of the POD mode coefficients,  $a_j(t)$ , in Eq. (12). The frequency characteristics of POD modes 1 ~ 4 in the  $(y, z)$  plane at  $x/W = 3$  are compared for both the STM and the CTM in Fig. 14a and b. As shown in Fig. 14a, multiple dispersive peaks exist for the first four modes of the STM in the  $(y, z)$  plane at  $x/W = 3$ . However, for the CTM, as shown in Fig. 14b, mode 1 and mode 2 exhibit the same dominant frequency of  $St_w = 0.16$  ( $St_w = fW/U$ ,  $W$  is the train width), which is the same as the frequency obtained from the instantaneous streamwise velocity, as shown in Fig. 10b. This implies that the first two modes may present different phases of one particular periodic motion.

In order to fully understand which coherent structure is associated with a certain mode, it might be difficult to only analyze a particular mode. As indicated by Eq. (11), the wake flow structures can be reconstructed by combining the mean velocity field and several lower POD modes representing reduced-order dynamics of the wake. Figure 15 a~d shows three typical sequential snapshots of the reconstructed flow field in the  $(y, z)$  plane at  $x/W = 3$  for each of the first four modes of the STM. According to the sequential snapshots, we can confirm the coherence of the first four modes as the following: Mode 1 represents simultaneous increase/decrease in size of the streamwise vortex pair. This corresponds to the streamwise connector strand in the half loop structure (see Fig. 9d). Mode 2 represents the simultaneous/homodromous spanwise motion of the streamwise vortex pair implying that the half-loop vortex has a spanwise oscillation. Mode 3 illustrates the simultaneous/symmetrical spanwise motion of the streamwise vortex pair. This corresponds to the passage of the half-loop vortex shown in Fig. 9. For example, as in Fig. 15c, at time T2, the vortex represents the section close to the centre line of the half-loop structure. At T3, it represents the section of the outside part of the streamwise connector strand. Mode 4 exhibits the simultaneous vertical motion of the streamwise vortex pair. This corresponds to the curved segment of the half-loop structure.

Three typical sequential snapshots of the reconstructed flow field for each of the first four modes in the  $(y, z)$  plane at  $x/W = 3$  for the CTM are shown in Fig. 16a~d. Comparing Fig. 15 and 16 the difference between the two underbody configurations in the mode pattern can be clearly noted. Based on the sequential snapshots, we can confirm the corresponding flow

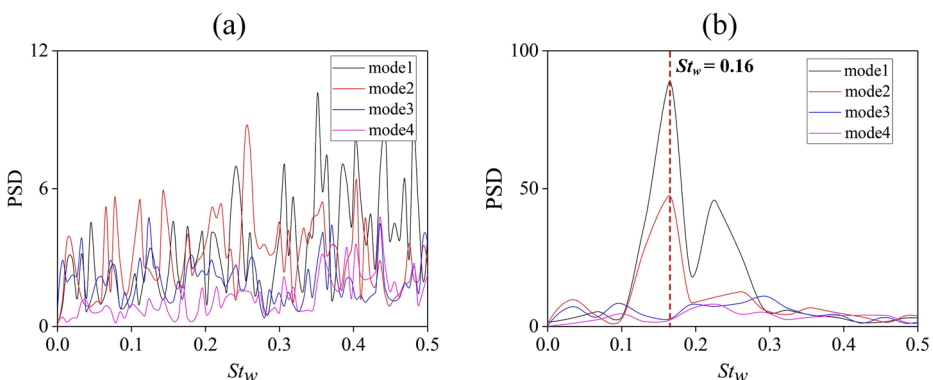


**Fig. 14** Power spectral density of the first four modes in the  $(y, z)$  plane at  $x/W = 3$ : (a) STM, (b) CTM



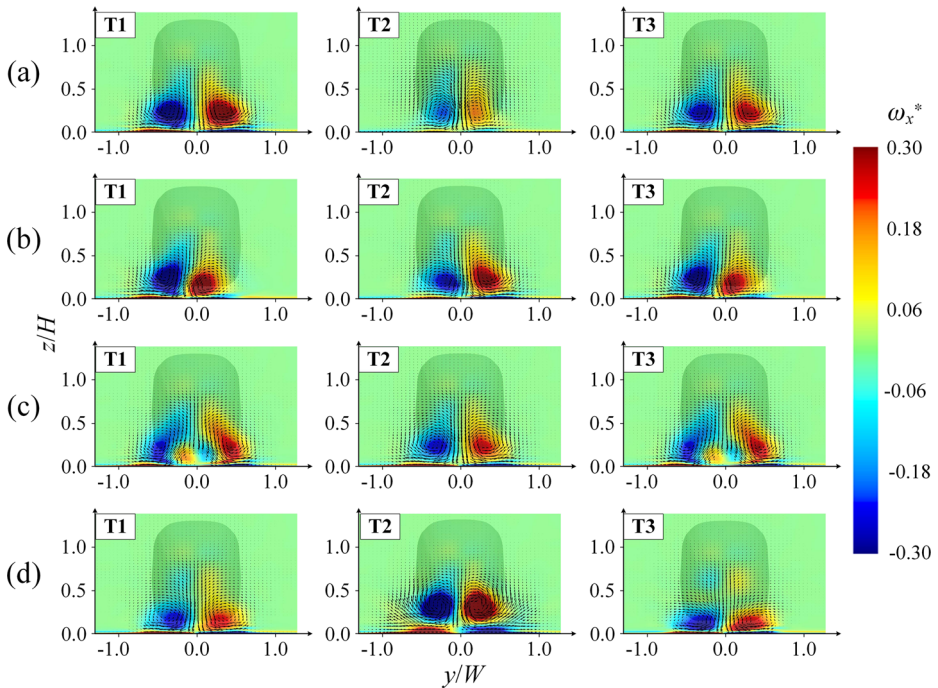


**Fig. 15** Reconstructed flow field in the  $(y, z)$  plane at  $x/W=3$  of the STM with velocity vector,  $(v, w)$ , and streamwise vorticity contour,  $\omega_x^*$ : **(a)** mode 1, **(b)** mode 2, **(c)** mode 3, **(d)** mode 4

structures of the first four modes in the CTM case as the following: Mode 1 represents an alternating out-of-phase increase/decrease in size and vorticity of the streamwise vortex pair and the induced secondary vortex structure. Mode 2 is similar to mode 1 except for the small difference in the shape and location of the vortices. Mode 1 and mode 2 correspond to the alternating half-loop vortex pair in different phases. Mode 3 illustrates the simultaneous appearance of the induced secondary vortex pair at the lower part of the wake. Mode 4 exhibits the simultaneous oscillation in the diagonal direction of the vortex pair.

### 3.3.2 Streamwise wake dynamics

Figure 17a and b show the first four POD modes in the  $(x, y)$  plane at  $z/W=0.12$  for the STM and the CTM, respectively, which are represented by the vertical vorticity contours,  $\omega_z^*$ , and velocity vectors,  $(u, v)$ .

For the STM, the first four modes only occupy 8.6% of the total TKE (see Fig. 12). Mode 1 ~ 4 contain 2.8%, 2.3%, 1.7% and 1.7%, respectively, of the total TKE implying that they have approximately the equivalent contribution to the wake in the plane at  $z/W=0.12$ . As shown in Fig. 17a, mode 1 and 2 look the same with an offset in the streamwise direction. The spectra for these two modes are very similar to each other with the same strong peak around  $Stw=0.12$  and 0.15 (see Fig. 18a), confirming the link between these two modes. Moreover, the cross-correlation results indicate that modes 1 and 2 are correlated and a phase shift of  $\pi/2$  from each other at  $Stw=0.12$  and 0.15, as shown in Fig. 19a. This implies that the two modes correspond to a flow structure. A connection also exists between modes 3 and 4. They have similar spatial structures and the same dominant frequency at  $Stw=0.39$  (see Figs. 17a, 18a and 19a). It can



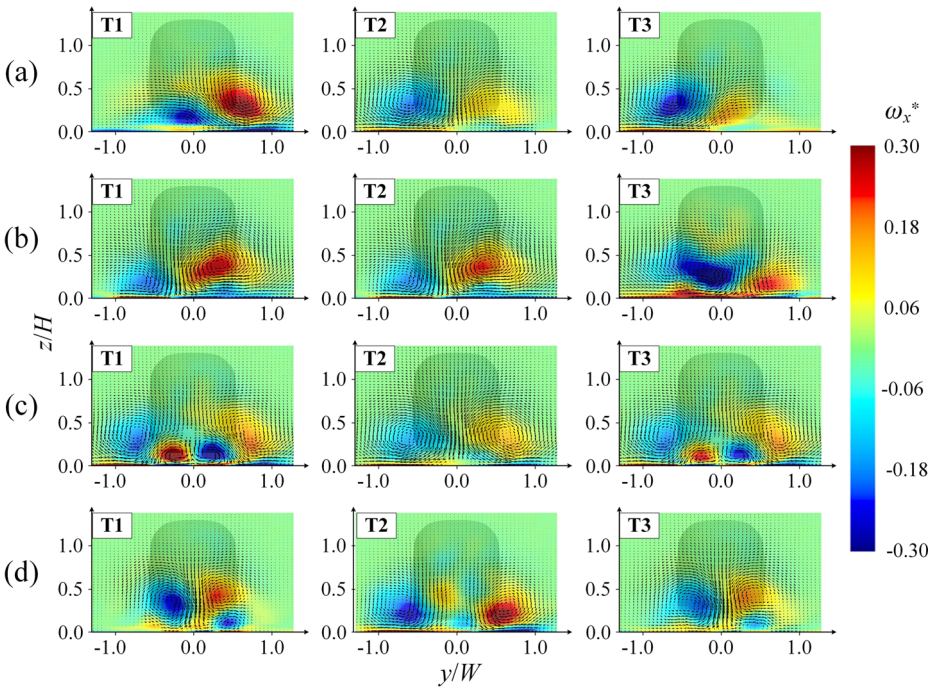


**Fig. 16** Reconstructed flow field in the  $(y, z)$  plane at  $x/W=3$  of the CTM with velocity vector,  $(v, w)$ , and streamwise vorticity contour,  $\omega_x^*$ : (a) mode 1, (b) mode 2, (c) mode 3, (d) mode 4

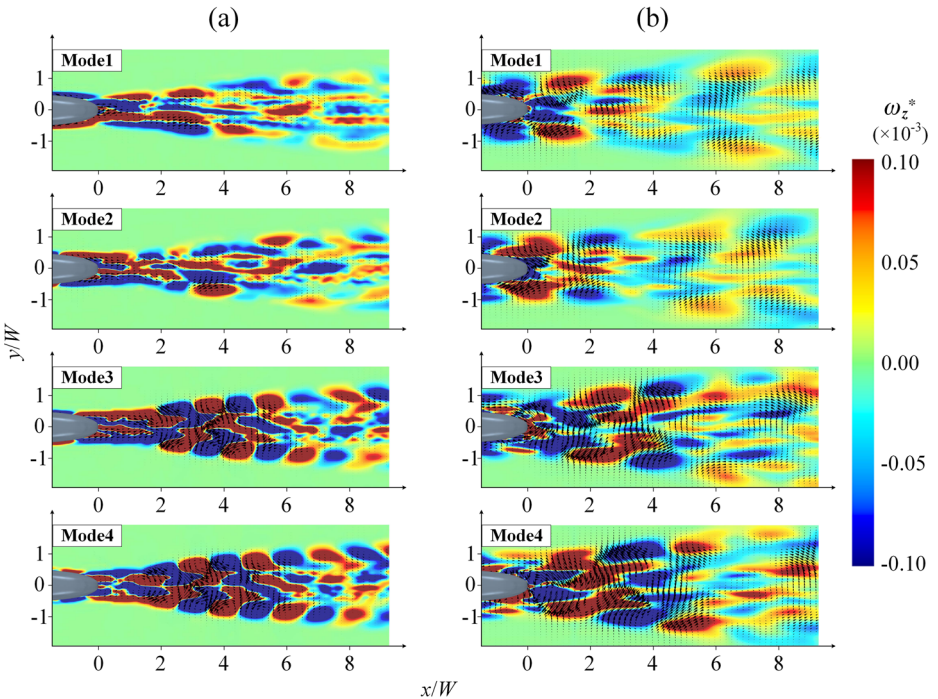


**Fig. 17** The first four modes in the  $(x, y)$  plane at  $z/W=0.12$ : (a) STM, (b) CTM

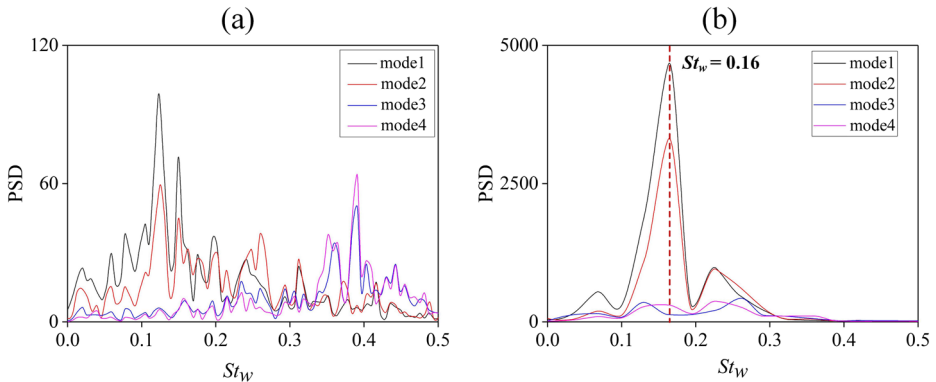


**Fig. 18** PSD of the first four modes in the  $(x, y)$  plane at  $z/W = 0.12$ : (a) STM, (b) CTM

also be found that peaks exist around the frequencies of  $St_w = 0.12$ ,  $0.15$  and  $0.39$  in the PSD of the instantaneous velocity (see Fig. 10a), and the phase shift is approximately zero around these frequencies (see Fig. 11a).

For the CTM, the first four modes contribute 27.6% of the total TKE energy. Meanwhile, the first two modes with a significant total contribution up to 21.8% (see Fig. 12) are clearly dominant with similar energy fractions (12.3% and 9.5%), which is 16.7% higher than that of the STM. However, mode 3 and mode 4 only contribute 3% and 2.8%, respectively, as illustrated in Fig. 12. Moreover, the flow patterns of the first two modes are quite similar except for a  $\pi/2$  phase shift, as shown in Fig. 19b. In addition, the temporal coefficients of the first two modes also share the same dominant Strouhal number of  $St_w = 0.16$ , as shown in Fig. 18b. The phase shift between the two temporal coefficients is approximately  $\pi/2$  (see Fig. 19b) indicating that the first two modes correspond to the different phases of a periodic flow structure. This feature is the same as the famous Von Karman vortex shedding behind a two-dimensional cylinder. Nevertheless, the absolute energy content of the first two modes is much lower due to the highly three-dimensionally characteristics behind a HST compared to the corresponding value in a 2D cylinder wake. In addition, the forms of the second pair of modes (mode 3 and mode 4) are also quite similar, as illustrated in Fig. 19b.

Figure 20a and b present three typical sequential snapshots of the reconstructed flow field for the first pair of modes (mode 1 and mode 2) and the second pair of modes (mode 3 and mode 4) in

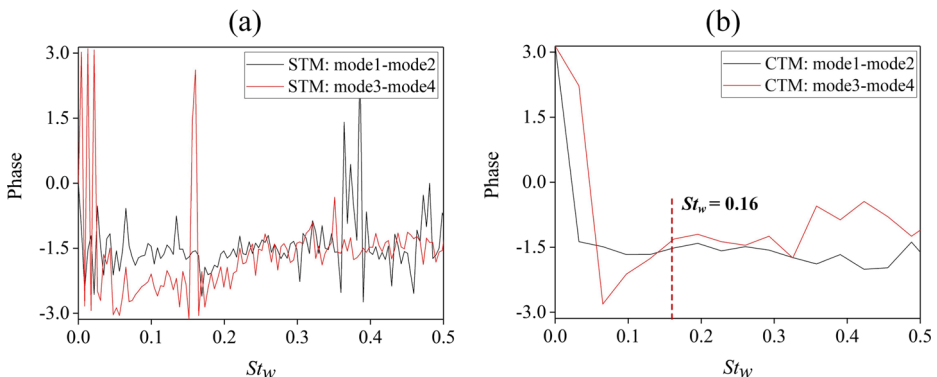


**Fig. 19** Cross spectrum (phase shift) of the first four modes in the  $(x, y)$  plane at  $z/W = 0.12$ : (a) STM, (b) CTM

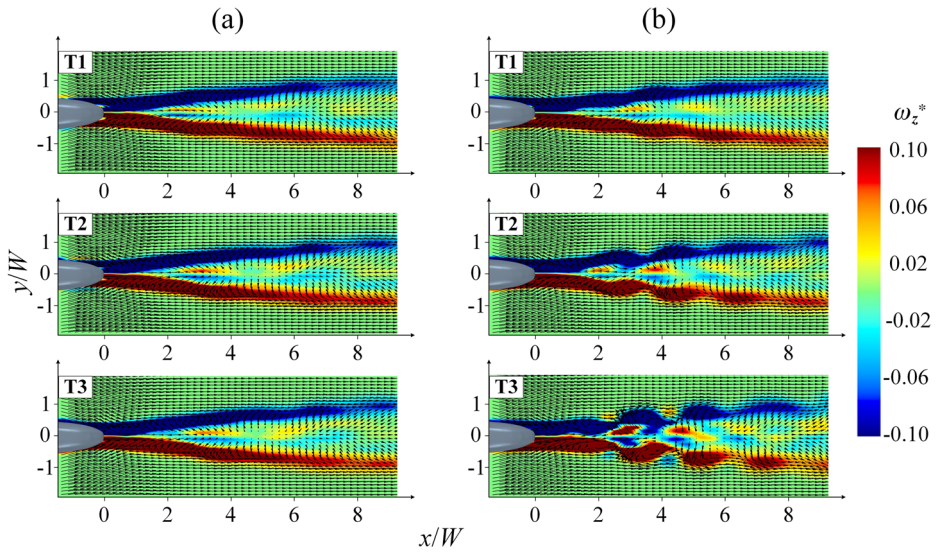


**Fig. 20** Reconstructed flow field in the  $(x, y)$  plane at  $z/W=0.12$  of the STM with velocity vector,  $(u, v)$ , and vertical vorticity contours,  $\omega_z^*$ : (a) the first pair of modes (mode 1 and 2), (b) the second pair of modes (mode 3 and 4)

the  $(x, y)$  plane at  $z/W = 0.12$  for the STM, respectively, presented by the vertical vorticity,  $\omega_z^*$ , and velocity vectors,  $(u, v)$ . The first pair of modes represent the simultaneous/symmetrical spanwise oscillation of the shear layer with sinusoidal motion occurring at  $Stw = 0.12$  in the wake, as shown in Fig. 20a. The second pair represents simultaneous/symmetrical vortex shedding from both sides of the shear layers at  $Stw = 0.39$ , as illustrated in Fig. 20b. The dominant vortex shedding corresponds to the principal core of the half-loop vortex shown in Fig. 9.

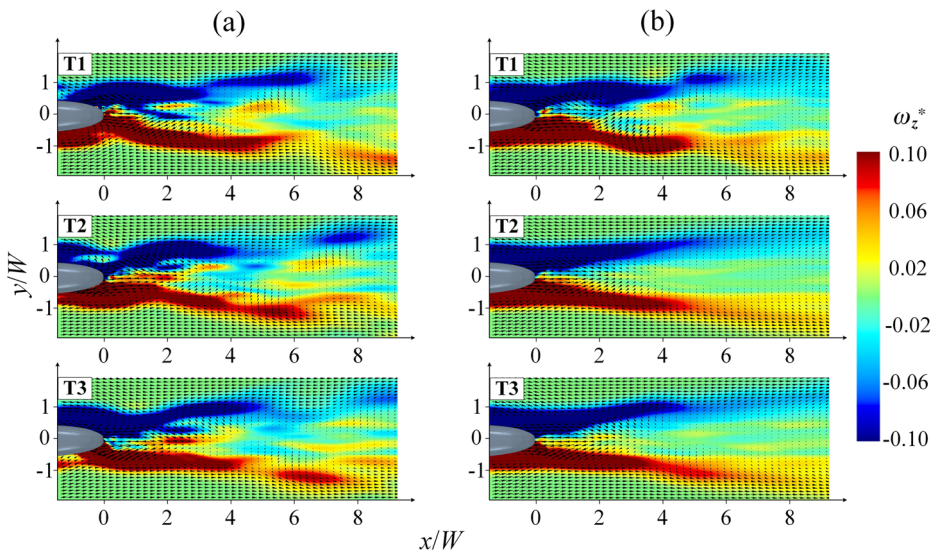


**Fig. 21** Reconstructed flow field with velocity vector  $(u, v)$ , and vertical vorticity contour,  $\omega_z^*$ , in the  $(x, y)$  plane at  $z/W=0.12$  of the CTM: (a) the first pair of modes (mode 1 and 2), (b) the second pair of modes (mode 3 and 4)

The reconstructed flow fields (three typical snapshots) for two pairs of modes (mode 1 and 2 & mode 3 and 4) in the  $(x, y)$  plane at  $z/W=0.12$  for the CTM are shown in Fig. 21a and b, respectively, demonstrating distinct wake dynamics from that of the STM shown in Fig. 20. As illustrated in Fig. 21a, the first pair of modes (mode 1 and 2) represent an alternating slender vortex shedding generated from the left or right side shear layers. This is the dominant vortex structures in the wake of the CTM occurring at  $St_w=0.16$  (Fig. 19b and 21b), which is consistent with the spectrum of instantaneous streamwise velocity signals (see Fig. 10) and the spectrum of the first pair of modes in the  $x/W=3$  plane of the CTM (see Fig. 14b). The second pair of modes (mode 3 and 4) exhibits bi-stable behaviour, i.e., transforming between alternating vortex shedding and a sinusoidal spanwise swing, which has also been observed in one of our previous experiments [18].

## 4 Conclusions

The wake dynamics of a 1/50th scale CRH3 HST with two underbody configurations, i.e., the complex train model (CTM) with bogie sections and the simplified train (STM) with a flat underbody, are numerically compared using IDDES. Focus is placed on the spatial-temporal evolution of the unsteady wake. POD is successfully utilized in the description of the unsteady wake dynamics of the HSTs, which provides clearer observations on the differences between the unsteady wake topology behind the CTM and the STM. Based on the above analysis, the following conclusions can be drawn:

1. A pair of symmetric counter-rotating streamwise vortices in the wake are exhibited for both the CTM and the STM in view of the time-averaged flow field. However, the streamwise vortices of the CTM have larger sizes and have a larger distance between the two vortex cores relative to that of the STM. In addition, the streamwise vortex in the CTM case presents a more rapid vorticity diffusion when moving downstream compared to the STM case.
2. A pair of counter-rotating half-loop vortices dominates the unsteady wake for both underbody configurations. Each member of the vortex pair sheds alternately in the wake of the CTM, which is attributed to vortex shedding originating from the bogie section of the tail. However, for the STM, this vortex pair is coupled and the two vortices in the pair appear simultaneously.
3. Utilizing POD analysis, the spatial-temporal evolution of the wake is clarified. Based on the spectrum of the mode coefficients and reconstructed wake flow, the first four POD modes corresponding to the dominant vortex structures are described in detail, confirming the significant impact of bogie sections on the wake dynamics of a HST.

**Acknowledgements** This work was supported by the National Natural Science Foundation of China (Grand No. 51875411), Shanghai Key Laboratory of Aerodynamics and Thermal Environment Simulation for Ground Vehicles (Grand No. 18DZ2273300) and Shanghai Automotive Wind Tunnel Technical Service Platform (Grand No. 19DZ2290400). The computing facility and aero-acoustic wind tunnel of Shanghai Key Lab of Vehicle Aerodynamics and Vehicle Thermal Management Systems is gratefully acknowledged.



## Compliance with Ethical Standards

**Conflict of Interests** The authors declare that they have no conflict of interest.

**Abbreviations**  $St_w$ , Strouhal number;  $f$ , The frequency;  $D$ , The hydraulic diameter;  $U^*$ , The streamwise velocity;  $W$ , The train width;  $U_\infty$ , The oncoming flow velocity;  $u^*$ , The friction velocity;  $n$ , The distance between the first node and the train surface in the wall normal direction;  $\Delta l$ , The cell width in the streamwise direction;  $\Delta s$ , The cell width in the spanwise direction;  $h_{wb}$ , The grid step in the wall-normal direction;  $C_w$ , An empirical constant;  $h_{max}$ , The largest local grid spacing;  $h_x$ , Local streamwise cell size;  $h_y$ , Local wall-normal cell size;  $h_z$ , Local lateral cell size;  $t^*$ ,  $t^* = H/U_\infty$ ;  $C_D$ , The drag force coefficient;  $F_D$ , The drag force;  $\rho$ , The density of the air;  $A_x$ , The projected area in the  $x$  direction;  $C_B$ , The pressure coefficient;  $P$ , The time-averaged surface pressure;  $P_\infty$ , The static pressure;  $u$ , The velocity in the X direction;  $v$ , The velocity in the Y direction;  $w$ , The velocity in the Z direction;  $U_{mean}$ , Time-averaged  $x$ -direction velocity;  $V_{mean}$ , Time-averaged  $y$ -direction velocity;  $U_{RMS}$ ,  $x$ -direction velocity fluctuation;  $V_{RMS}$ ,  $y$ -direction velocity fluctuation  $V_{RMS}$ ;  $\omega_x^*$ ,  $x$ -direction vorticity;  $\omega_z^*$ ,  $z$ -direction vorticity;  $a_j$ , The temporal coefficients of the POD modes

## References

1. Baker, C.J.: The flow around high speed trains. *J. Wind Eng. Ind. Aerodyn.* **98**(6), 277–298 (2010). <https://doi.org/10.1016/j.jweia.2009.11.002>
2. Bell, J.R., Burton, D., Thompson, M., Herbst, A., Sheridan, J.: Wind tunnel analysis of the slipstream and wake of a high-speed train. *J. Wind Eng. Ind. Aerodyn.* **134**, 122–138 (2014). <https://doi.org/10.1016/j.jweia.2014.09.004>
3. Bell, J.R., Burton, D., Thompson, M.C., Herbst, A.H., Sheridan, J.: Dynamics of trailing vortices in the wake of a generic high-speed train. *J. Fluid. Struct.* **65**, 238–256 (2016). <https://doi.org/10.1016/j.jfluidstructs.2016.06.003>
4. Bell, J.R., Burton, D., Thompson, M.C., Herbst, A.H., Sheridan, J.: Flow topology and unsteady features of the wake of a generic high-speed train. *J. Fluid. Struct.* **61**, 168–183 (2016). <https://doi.org/10.1016/j.jfluidstructs.201511.009>
5. Xia, C., Wang, H.F., Shan, X.Z., Yang, Z.G., Li, Q.L.: Effects of ground configurations on the slipstream and near wake of a high-speed train. *J. Wind Eng. Ind. Aerodyn.* **168**, 177–189 (2017). <https://doi.org/10.1016/j.jweia.2017.06.005>
6. Pope, C.W., 2007, "Effective Management of Risk from slipstream effects at trackside and platforms," Rail Safety and Standards Board – T425 Report
7. Baker, C.J., Quinn, A., Sima, M., Hoefener, L., Licciardello, R.: "Full-scale measurement and analysis of train slipstreams and wakes," part 1: ensemble averages. *Proc. Inst. Mech. Eng. Part F: J. Rail Rapid Transp.* **228**(5), 451–467 (2014). <https://doi.org/10.1177/0954409713485944>
8. Baker, C.J., Quinn, A., Sima, M., Hoefener, L., Licciardello, R.: "Full-scale measurement and analysis of train slipstreams and wakes," part 2: gust analysis. *Proc. Inst. Mech. Eng. Part F: J. Rail Rapid Transp.* **228**(5), 468–480 (2014). <https://doi.org/10.1177/0954409713488098>
9. Baker, C.J., Dalley, S.J., Johnson, T., Quinn, A., Wright, N.G.: The slipstream and wake of a high-speed train. *Proc. Inst. Mech. Eng. Part F: J. Rail Rapid Transp.* **215**(2), 83–99 (2001). <https://doi.org/10.1243/0954409011531422>
10. Gilbert, T., Baker, C.J., Quinn, A.: Gusts caused by high-speed trains in confined spaces and tunnels. *J. Wind Eng. Ind. Aerodyn.* **121**, 39–48 (2013). <https://doi.org/10.1016/j.jweia.2013.07.015>
11. Weise, M., Schober, M., Orellano, A.: Slipstream velocities induced by trains. *WSEAS Transactions on Fluid Mechanics.* **1**(6), 759–761 (2006)
12. Schulte-Werning, B., Heine, B., Matschke, C.: Unsteady wake flow characteristics of high-speed trains. *Proc. Appl. Maths Mech.* **2**(1), 332–333 (2003)
13. Muld, T.W., Efraimsson, G., Henningson, D.S.: Flow structures around a HST extracted using proper orthogonal decomposition and dynamic mode decomposition. *Comput. Fluids.* **57**, 87–97 (2012). <https://doi.org/10.1016/j.compfluid.2011.12.012>
14. Pii, L., Vanoli, E., Polidoro, F., Gautier, S., and Tabbal, A., 2014, "A Full Scale Simulation of a High Speed Train for Slipstream Prediction," in: Proceedings of the Transport Research Arena, Paris, France

15. Östth, J., Kaiser, E., Krajnović, S., Noack, N.R.: Cluster-based reduced-order modelling of the flow in the wake of a high speed train. *J. Wind Eng. Ind. Aerodyn.* **145**, 327–338 (2015). <https://doi.org/10.1016/j.jweia.2015.06.003>
16. Wang, S.B., Burton, d., Herbst, A., Sheridan, J., Thompson, M.C.: The effect of bogies on high-speed train slipstream and wake. *J. Fluids Struct.* **83**, 471–489 (2018). <https://doi.org/10.1016/j.jfluidstruct.2018.03.013>
17. Xia, C., Shan, X.Z., Yang, Z.G.: Detached-Eddy simulation of ground effect on the wake of a high-speed train. *J. Fluids Eng.* **139**(5), 1–12 (2017). <https://doi.org/10.1115/1.4035804>
18. Xia, C., Wang, H.F., Bao, D., Yang, Z.G.: Unsteady flow structures in the wake of a high-speed train. *Exp. Thermal Fluid Sci.* **98**, 381–396 (2018). <https://doi.org/10.1016/j.expthermflusci.2018.06.010>
19. Bourgeois, J.A., Sattari, P., Martinuzzi, R.J.: Alternating half-loop shedding in the turbulent wake of a finite surface-mounted square cylinder with a thin boundary layer. *Phys. Fluids.* **23**(9), 095101 (2011). <https://doi.org/10.1063/1.3623463>
20. Wang, S.B., Bell, J.R., David, B., Herbst, A.H., Sheridan, J., Thompson, M.C.: The performance of different turbulence models (URANS, SAS and DES) for predicting HST slipstream. *J. Wind Eng. Ind. Aerodyn.* **165**, 46–65 (2017). <https://doi.org/10.1016/j.jweia.2017.03.001>
21. Tschepe, J., Fischer, D., Nayeri, C.N., Paschereit, C.O., Krajnovic, S.: Investigation of high-speed train drag with towing tank experiments and CFD. *Flow, Turbulence and Combustion.* **102**, 1–18 (2018). <https://doi.org/10.1007/s10494-018-9962-y>
22. Morden, J.A., Hemida, H., Baker, C.J.: Comparison of RANS and detached eddy simulation results to wind-tunnel data for the surface pressures upon a class 43 high-speed train. *J. Fluids Eng.* **137**(4), 1–9 (2015). <https://doi.org/10.1115/1.4029261>
23. Rao, A.N., Zhang, J., Minelli, G., Basara, B., Krajnović, S.: An LES investigation of the near-wake flow topology of a simplified heavy vehicle. *Flow, Turbulence and Combustion.* **102**, 1–27 (2018). <https://doi.org/10.1007/s10494-018-9959-6>
24. Shur, M.L., Spalart, P.R., Strelets, M.K., Travin, A.K.: A hybrid RANS-LES approach with delayed-DES and wall-modelled LES capabilities. *Int. J. Heat Fluid Flow.* **29**(6), 1638–1649 (2008). <https://doi.org/10.1016/j.ijheatfluidflow.2008.07.001>
25. Spalart, P.R.: Detached-eddy simulation. *Ann. Rev. Fluid Mech.* **41**(1), 181–202 (2009). <https://doi.org/10.1146/annurev.fluid.010908.165130>
26. Huang, S., Hemida, H., Yang, M.Z.: Numerical calculation of the slipstream generated by a CRH2 high-speed train. *Proc. Inst. Mech. Eng. Part F: J. Rail Rapid Transp.* **230**(1), 103–116 (2016)
27. Travin, A., Shur M.L., Strelets M.K. and Spalart, P.R., 2000, "Physical and numerical upgrades in the detached-eddy simulation of complex turbulent flows," In Proceedings of the 412th Euromech Colloquium on LES and Complex Transitional and Turbulent Flows, Munich, Germany
28. Flynn, D., Hemida, H., Soper, D., Baker, C.J.: Detached-eddy simulation of the slipstream of an operational freight train. *J. Wind Eng. Ind. Aerodyn.* **132**, 1–12 (2014). <https://doi.org/10.1016/j.jweia.2014.06.016>
29. Flynn, D., Hemida, H., Baker, C.J.: On the effect of crosswinds on the slipstream of a freight train and associated effects. *J. Wind Eng. Ind. Aerodyn.* **156**, 14–28 (2016). <https://doi.org/10.1016/j.jweia.2016.07.001>
30. Sirovich, L.: Turbulence and the dynamics of coherent structures part I: coherent structures. *Q. Appl. Math.* **45**(3), 561–571 (1987)
31. Taira, K., Brunton, S.L., Dawson, S.T., Rowley, C.W., Colonius, T., McKeon, B.J., Schmidt, O.T., Gordeyev, S., Theofilis, V., Ukeiley, L.S.: Modal analysis of fluid flows: an overview. *AIAA J.* **55**(12), 4013–4041 (2017). <https://doi.org/10.2514/1.J056060>
32. Wang, H.F., Cao, H.L., Zhou, Y.: POD analysis of a finite-length cylinder near wake. *Exp. Fluids.* **55**(8), (2014). <https://doi.org/10.1007/s00348-014-1790-9>
33. Zhu, H.Y., Wang, C.Y., Wang, H.P., Wang, J.J.: Tomographic PIV investigation on 3D wake structures for flow over a wall-mounted short cylinder. *J. Fluid Mech.* **831**, 743–778 (2017). <https://doi.org/10.1017/jfm.2017.647>
34. Wei, Z., Yang, Z.G., Xia, C., Li, Q.L.: Cluster-based reduced-order modelling of the wake stabilization mechanism behind a twisted cylinder. *J. Wind Eng. Ind. Aerodyn.* **171**, 288–303 (2017). <https://doi.org/10.1016/j.jweia.2017.10.015>
35. Hemida, H., Baker, C.J., Gao, G.: The calculation of train slipstreams using large-eddy simulation. *Proc. Inst. Mech. Eng. Part F: J. Rail Rapid Transp.* **228**(1), 25–36 (2013). <https://doi.org/10.1177/0954409712460982>
36. Yao, S.B., Sun, Z.X., Guo, D.L., Chen, D.W., Yang, G.W.: Numerical study on wake characteristics of high-speed trains. *Acta Mech. Sinica.* **29**(6), 811–822 (2013). <https://doi.org/10.1007/s10409-013-0077-3>
37. Jeong, J., Hussain, F.: On the identification of a vortex. *J. Fluid Mech.* **285**, 69–94 (1995). <https://doi.org/10.1017/S0022112095000462>

38. Hosseini, Z., Bourgeois, J.A., Martinuzzi, R.J.: Large-scale structures in dipole and quadrupole wakes of a wall-mounted finite rectangular cylinder. *Exp. Fluids*. **54**(9), 1–16 (2013). <https://doi.org/10.1007/s00348-013-1595-2>
39. Saeedi, M., Lepoudre, P.P., Wang, B.C.: Direct numerical simulation of turbulent wake behind a surface-mounted square cylinder. *J. Fluid Struct.* **51**, 20–39 (2014). <https://doi.org/10.1016/j.jfluidstructs.2014.06.021>
40. Saeedi, M., Wang, B.C.: Large-eddy simulation of turbulent flow around a finite-height wall-mounted square cylinder within a thin boundary layer. *Flow Turbul. Combust.* **97**(2), 513–538 (2016). <https://doi.org/10.1007/s10494-015-9700-7>
41. Pan, Y.C., Yao, J.W., Li, C.F.: Discussion on the wake vortex structure of a high speed train by vortex identification methods. *Chinese Journal of Theoretical and Applied Mechanics*. **50**(3), 667–676 (2018)
42. Niu, J.Q., Wang, Y.M., Zhang, L., Yuan, Y.P.: Numerical analysis of aerodynamic characteristics of high-speed train with different train nose lengths. *Int. J. Heat Mass Transf.* **127**, 188–199 (2018). <https://doi.org/10.1016/j.ijheatmasstransfer.2018.08.041>